Supporting Information

Fukuda et al. 10.1073/pnas.1701367114

SI Materials and Methods

Cell Culture and Sample Preparation. Primary neuron culture was carried out as described by Kaech and Banker (28) with some modifications. Gold Quantifoil grids (R1/4, Au 200 mesh, Quantifoil Micro Tools) were used as a substrate for neuronal cell cultivation. Before use, the grids were cleaned by floating them on acetone. Then, additionally, carbon (~25 nm) was deposited on the grids using a carbon evaporator (MED 020, BALTEC). Next, grids were sterilized by UV irradiation for 30 min and immersed in 1 mg/mL poly-L-lysine/0.1 M borate buffer (pH 8.5) in the dark overnight. After poly-L-lysine coating, grids were washed with autoclaved distilled water and soaked in neuronal plating medium in a CO_2 incubator until used for cell culture.

Neurons were isolated from the hippocampi of 2-d postnatal rats. The tissues were immersed in cold HBSS–Hepes, minced with a razor blade, trypsinized, and filtered with a cell strainer (Becton Dickinson). Collected cells were suspended in neuronal plating medium, and 4.0×10^5 cells were seeded in 35-mm-diameter petri dishes with four rings, each holding one prepared grid. The cells were cultivated in a CO_2 incubator for ~4 h. Then the grids were transferred to the grid holder in a 60-mm-diameter culture dish containing preconditioned Neurobasal-A/B27 medium and a glial feeder cell layer. Three days after seeding, Ara-C was added (final 5 μM) to the culture dish to stop glial cell duplication. Neurons were cultivated for 18 d. One-third of the culture medium was exchanged once per week.

Neurons cultivated on grids were plunge-frozen in a liquid ethane/propane mixture at close to liquid nitrogen temperature using a Vitrobot (FEI). As fiducial markers for tomographic reconstruction, 4 μL of four times concentrated BSA-coated gold nano particle solution (Aurion 10 nm BSA-coated gold) was dropped on the back side of the grid. The Vitrobot blotting chamber conditions were set to 37 °C, 90% humidity; waiting time was 5 s, and blot time was 10 s. After plunging, excess ethane/propane mixture was blotted from the grid using a small piece of filter paper in the liquid nitrogen surrounding the ethane cup. Grids were stored in liquid nitrogen until use.

Cryo-Electron Tomography. Cryo-electron tomography was performed on a Titan Krios (FEI) operated at an acceleration voltage of 300 kV. The Titan Krios was equipped with a field-emission gun, Gatan postcolumn energy filter, and a FEI Volta phase plate. Data were recorded using a direct detector camera (K2 summit, Gatan) operated in counting mode. Tilt series were collected using SerialEM (33). Tomographic tilt-series images were collected with the following parameters: magnification 33,000×, resulting in a pixel size of 4.21 Å at the specimen level; tilt range ± 60°; tilt increment 2°; and total dose ~110 $e^-/Å^2$. For data acquisition, images were collected with −1 μm defocus.

To discard intensity outliers from the micrographs of the tilt series, high-intensity pixels beyond 10 SDs were replaced by their neighborhood values. Tilt series were aligned based on fiducial gold markers and localized using the IMOD package (34). Marker position optimization, image alignment (4 degrees of freedom per image: shifts, rotation, magnification), and weighted backprojection of the 3D volume were done in MATLAB using the AV3 (29) and TOM toolbox (30). The micrographs were low-pass filtered at the Nyquist frequency of the 3D reconstruction, depending on the volume.

Template Matching. A human tripeptidyl peptidase II homo-36-mer (EMD-2036) and homo-32-mer (EMD-2037) (15) were downloaded from The Electron Microscopy Data Bank (EMDB). To calibrate the voxel sizes between EMDB density maps (1.78 Å) and our dataset (4.21 Å), EM density maps from EMDB were rescaled to 162^3 voxel. Then these models were trimmed into 160^3 voxel. For template matching of eight-times-binned tomograms, these trimmed models were rescaled to 20^3 voxel.

To avoid template bias, a spherical volume (251 voxels, corresponding to 17.5% of the volume in TPPII 36-mer and 19.7% of the volume in TPPII 32-mer, respectively) was removed from the center of rescaled volumes by using masks. These reduced volumes were used as templates in eight-times-binned tomograms ($462 \times 462 \times 300$ pixel volume, (33.68 $Å^3$ per voxel) for template matching in PyTom (31, 32). The cytoplasmic regions of these tomograms were segmented manually in Amira (FEI), and constrained correlation peaks (29) were extracted within these segmented volumes. For each tomogram, the top 100 peaks from both templates were visually inspected, and particle lists containing positives were merged to remove duplicate particles. Subtomograms of 200^3 pixel volumes and 4.21-Å pixel size corresponding to the positive hits were reconstructed and used for subsequent analysis.

Subtomogram Alignment and Classification. As an initial alignment, three steps of subtomogram averaging were performed (Fig. S1*B*). First, subtomogram averaging was performed using FRM implemented in PyTom (23) with a sphere object as the initial reference and a spherical mask. Second, subtomogram averaging was performed using FRM with an oriented 20th iteration from first averaging as the reference and a spherical mask. Third, subtomogram averaging was performed using real space alignment (RSA) implemented in PyTom (31) with an oriented 20th iteration from second averaging as the reference and a spherical mask.

Based on the particle center in the 10th iteration from RSA, the particle center in each particle was compensated to correct for the displacement of the particle center derived from missing the central volumes in both templates. All particles were reconstructed in 200^3-pixel volumes in correspondence to the corrected particle center.

After particle center correction, three steps of subtomogram averaging were performed as fine alignment (Fig. S1*B*). First, subtomogram averaging after correction was performed using FRM with a sphere object as the initial reference and a spherical mask. The output from first alignment step was oriented and low-pass filtered to 70 Å. This processed map was used as a starting model for the second alignment step. A spherical mask was used for the second alignment. This procedure divides the dataset into two halves that are aligned independently and hence allow resolution determination according to the gold standard FSC (24). Third, subtomogram averaging was performed using FRM with gold standard and D2 symmetry application. The output from second alignment step was oriented, low-pass filtered to 70 Å and D2 symmetry applied. This processed map was used as a starting model for the third alignment step. A tight mask was used for the third alignment.

The spatial resolution of the 20th iteration of the subtomogram averaged density map from the third averaging was measured using FSC. As a resolution criterion, we used FSC = 0.5 for comparing with the external reference FSC = 0.143 for "gold standard FSC."

After the fine alignment, 3D auto-focus classification (25) with focused a spherical mask encompassing both ends of the averaged map was applied to divide the particles into six classes. Based on the size of the EM density map, particles classified into six classes

were integrated into TPPII 36-mer and TPPII 32-mer. After integration into each class, the TPPII 36-mer class and 32-mer class are aligned by FRM with gold standard and FRM, respectively. Then the TPPII 36-mer class and the 32-mer class were aligned by FRM with gold standard and D2 symmetry application and FRM with D2 symmetry application, respectively.

For visualization, positions as well as orientation of the TPPII were taken from the results given by the subtomogram averaging. Visualization of the subtomogram averages was performed by UCSF Chimera (35).

Distance Analysis of Spatial Distribution. All analysis steps were carried out using MatLab and the TOM toolbox with homemade scripts. To check if there is a spatial relationship between the positions of TPPII and the positions of the 26S proteasome, distances between TPPII and 26S were analyzed. For every TPPII inside one tomogram, all Euclidean distances to the 26S were calculated. This was repeated for all 42 tomograms, and the resulting distances were combined. From these combined 2,206 distances, a histogram with 35 bins was computed. To check if the observed distance distribution significantly differs from a random distribution, a simulation of the 42 tomograms was calculated. To do so for each tomogram, the same amounts of TPPII and 26S particles were randomly placed within a cell mask. Then analogs to the measured position distances between TPPII and 26S were calculated and combined. To estimate how much the distances can vary for different simulations, this was repeated 1,000 times. For each bin of the histogram, the mean value and the SD was computed. To address the influence of the occupiable volume (protein density) on the result of the simulation, masks were reduced by 0, 6, 10, 20, and 30% by cutting out a sphere in the center of the cell mask. The simulation with 6% removed agreed best the observed distances (Fig. S9, black arrows). For visualization, the simulated and the observed distance distributions were overlaid. For the error bars, a SD ± 3σ range was used.

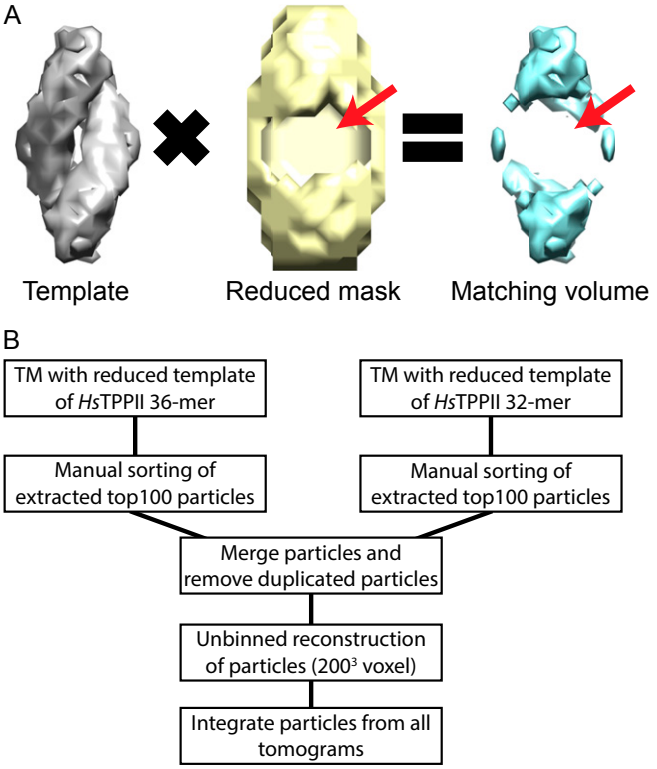

Fig. S1. Workflow of template matching for TPPII. (*A*) Volume reduction in mask for avoiding template bias. Reduced mask does not cover the whole template. Therefore, a reduced template was used for matching with cellular features. Arrows indicate empty volume that was computationally reduced. (*B*) Workflow for template matching to particle list creation.

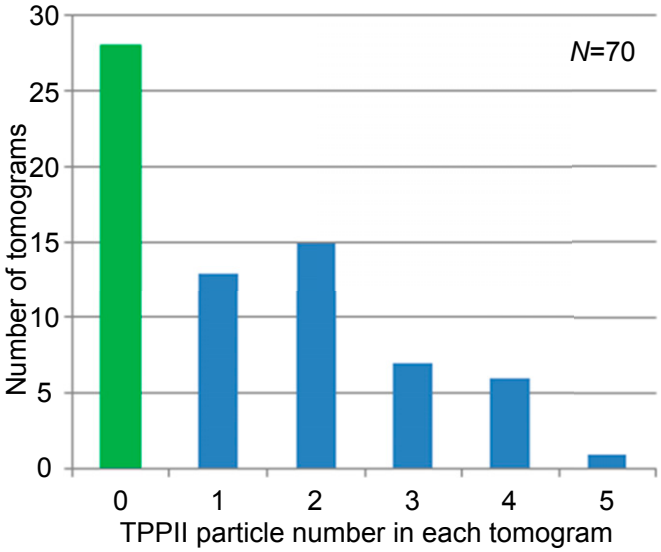

Fig. S2. Histogram of TPPII particle number in each tomogram. Template matchings of 70 tomograms provide 93 particles of TPPII. In the dataset, 28 tomograms (40%) contain no TPPII particle (green), 13 tomograms (18.6%) contain one particle, 15 tomograms (21.4%) contain two particles, 7 tomograms (10%) contain three particles, 6 tomograms (8.6%) contain four particles, and 1 tomogram (1.4%) contains five particles.

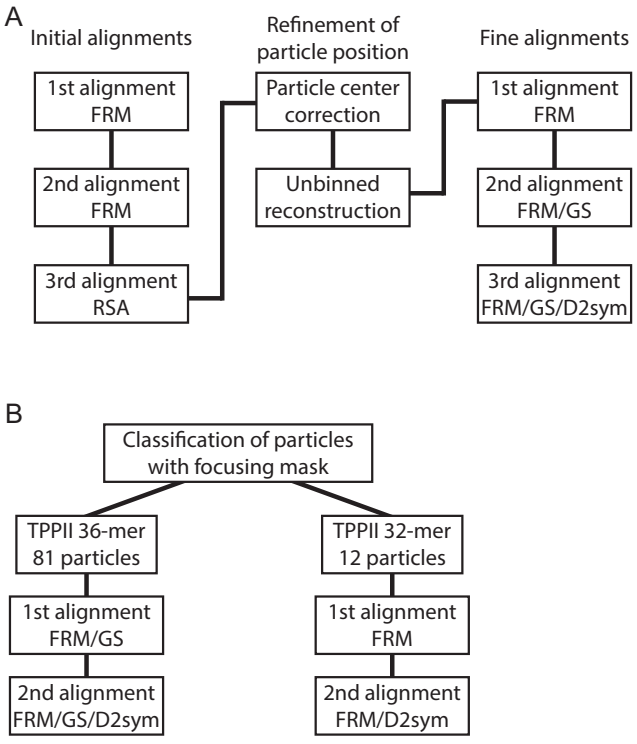

Fig. S3. Workflow for alignments. (*A*) Workflow of alignment processes for all particle alignments. (*B*) Workflow of alignment processes after classification. D2sym: Application of D2 symmetry; FRM, fast rotational matching, GS, gold standard; and RSA, real space alignment.

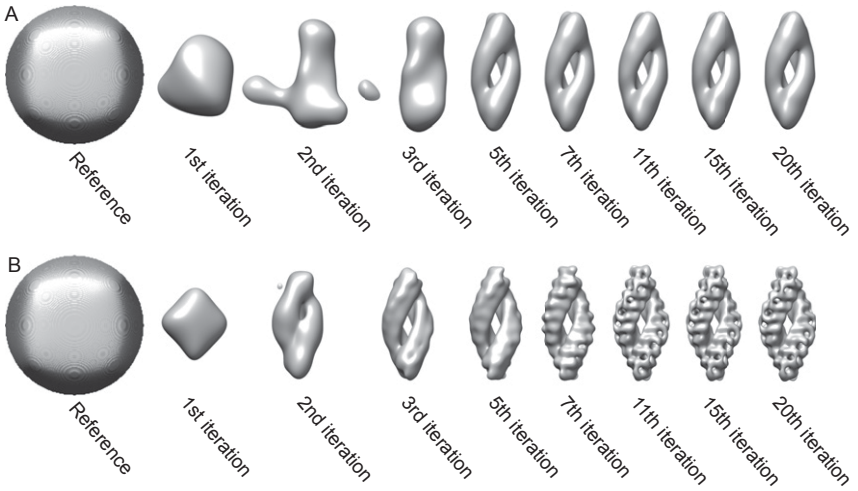

Fig. S4. Evolution of density during subtomogram averaging before and after particle recentering. The sphere reference is generated by TOM toolbox. Several iterations were selected to illustrate the convergence of the subtomogram averaged structure within 20 iterations (*Right*). (*A*) First alignment before particle recentering. (*B*) First alignment after particle recentering.

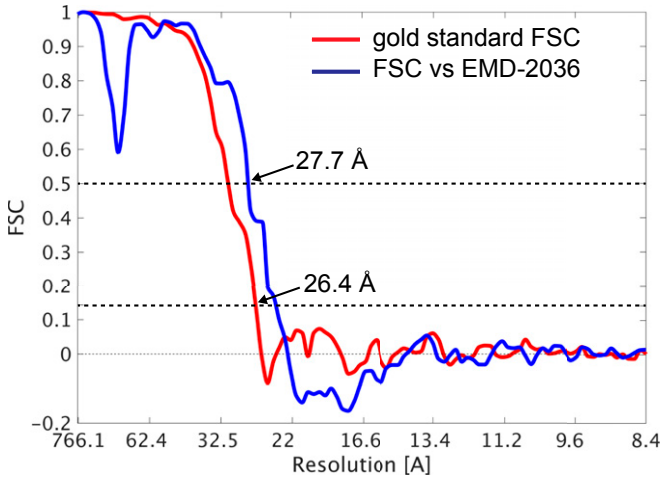

Fig. S5. Spatial resolution of TPPII in situ. The FSC curves from the internal gold standard (red line) and from a comparison with an external 9.9-Å density map (EMD-2036) (blue line). In gold standard, an averaged resolution of 26.4 Å is indicated at a 0.143 criterion. In a comparison with an external map, 27.7 Å is indicated at a 0.5 criterion. The Nyquist frequency is at 8.4 Å.

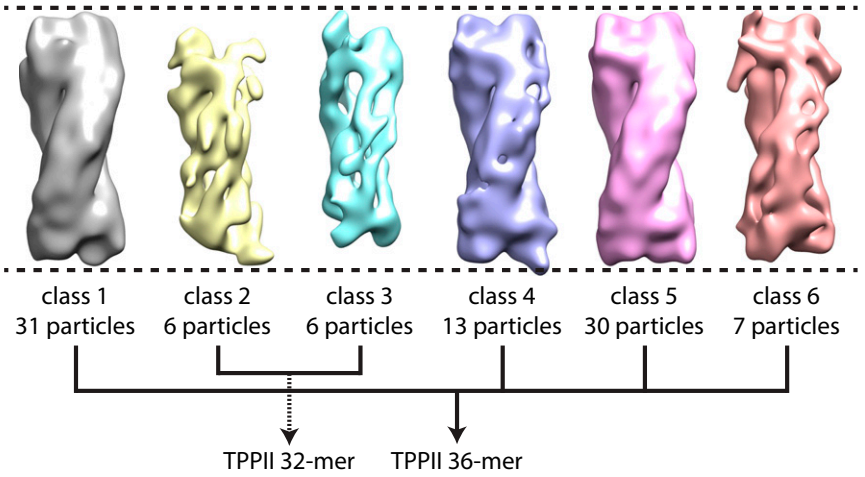

Fig. S6. Raw result of classification with focusing mask and integration into two classes. After the classification into six classes, all models were aligned to the class 1 model. According to the size of each model, classes 1, 4, 5, and 6 are integrated as a TPPII 36-mer. Classes 2 and 3 are integrated as a TPPII 32-mer.

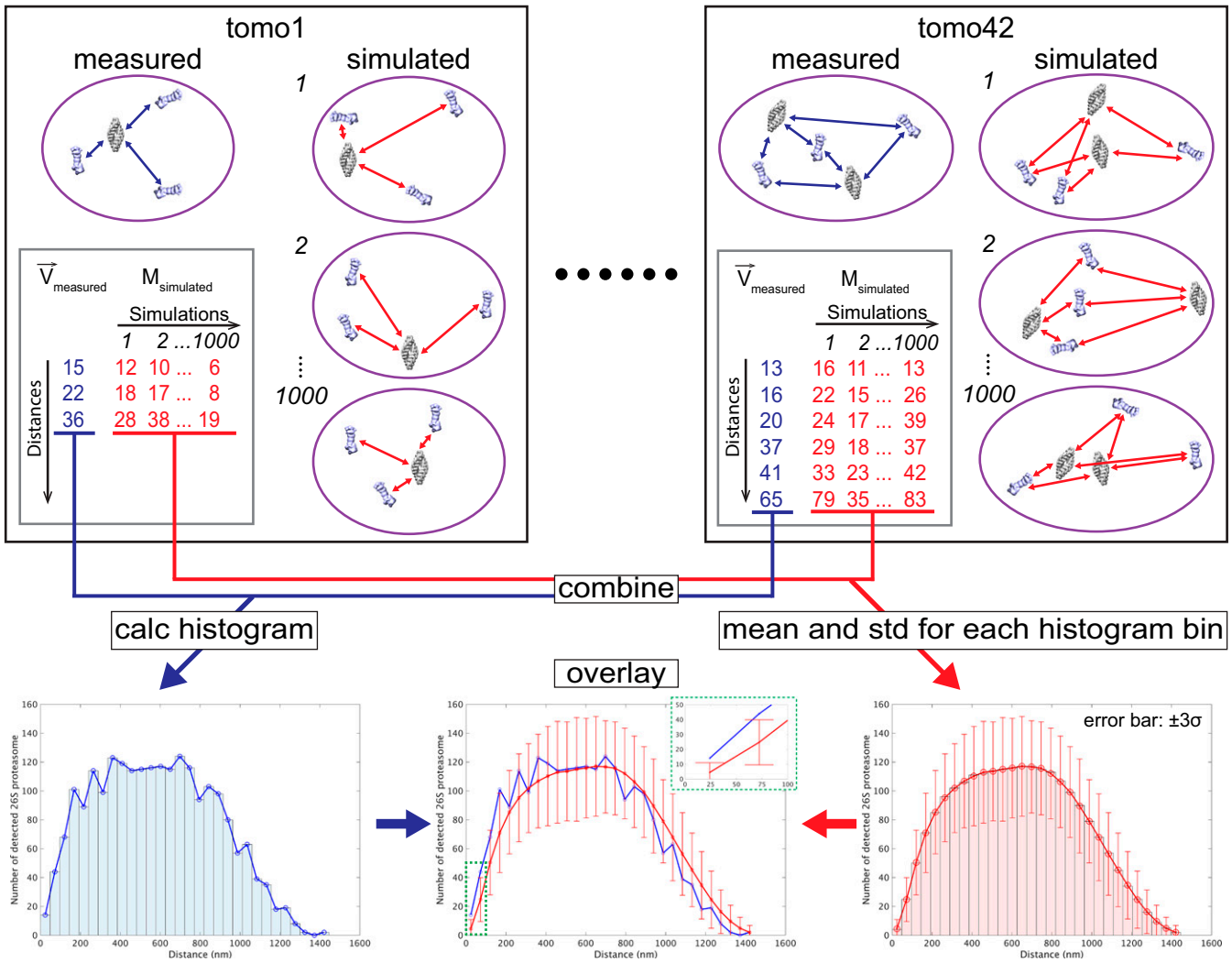

Fig. S7. Scheme of spatial relation analysis between TPPII and 26S proteasome. The distances from TPPII complexes to all 26S proteasomes were measured in all tomograms (blue double-headed arrows). All measured distances (blue digits) were combined, and a histogram was calculated (*Left Bottom*). For the simulation, an equal number of coordinate points corresponding to TPPII and 26S proteasomes was randomly distributed in a cellular region corresponding to the same volume used for template matching. Then distances between simulated TPPII and 26S proteasomes were measured (red double-headed arrows). The simulation was repeated 1,000 times. All obtained distances from simulations (red digits) were combined, and the mean and SD were calculated for all histogram bins (*Right Bottom*). Both histograms, measured and simulated, were overlaid (*Middle Bottom*). *Inset* plot is region of interest indicated by green dashed line in overlaid plots.

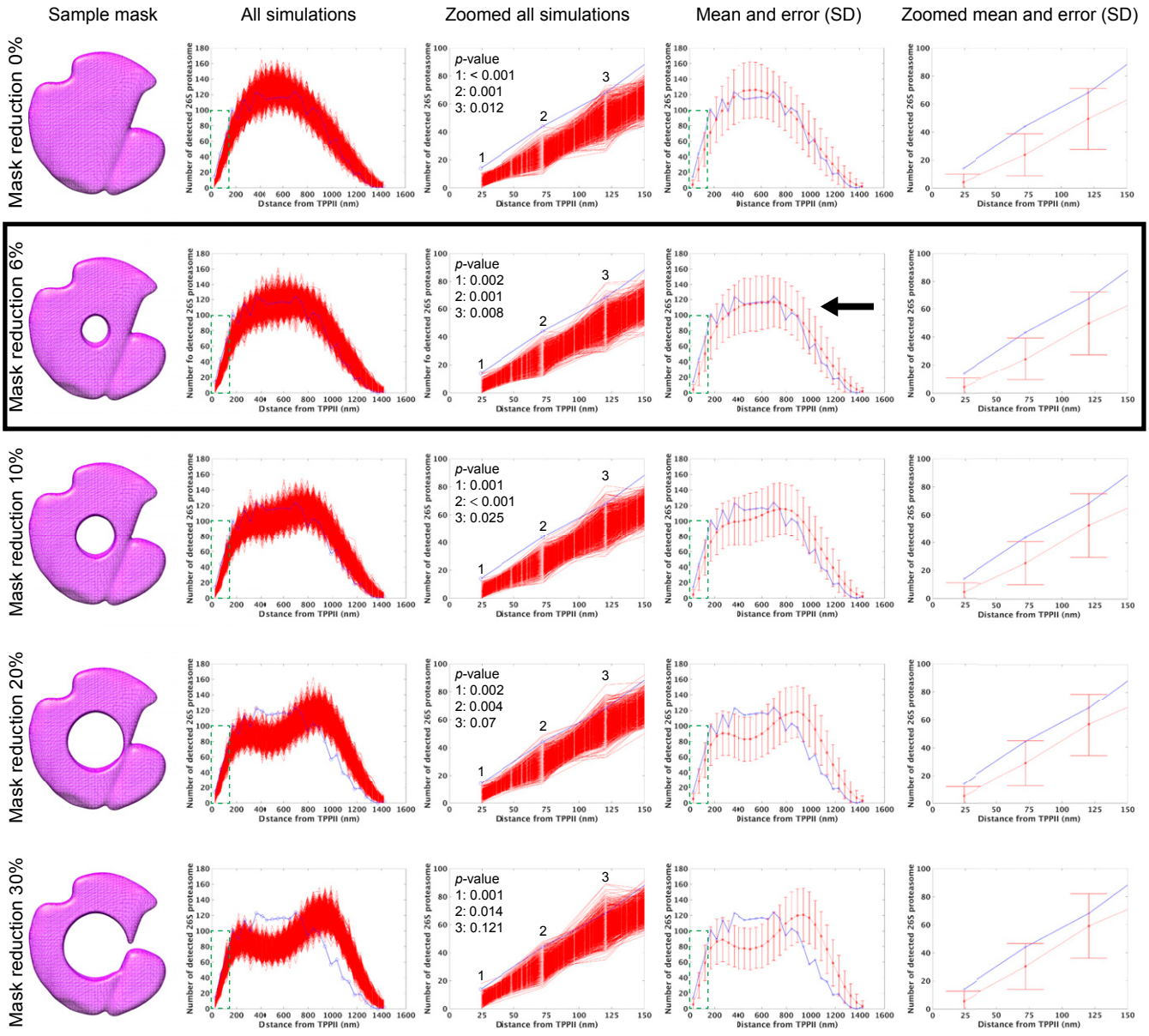

Fig. S8. Relation between occupiable volume (protein density) and distance distribution. (*Left* column) Examples of a mask with volume reduction. (Second from *Left* column) All plots from 1,000 times simulation (red). (*Middle* column) Zoomed area indicated by green dashed lines in second from *Left* column. *Inset* indicates *P* values at the first three bins. (Second from *Right* column) Mean and error bar of SD (red). Error bars of SD indicate $\pm 3\sigma$ range. Blue lines in histograms are measured distances. (*Right* column) Zoomed area indicated by green dashed lines in second from *Right* column. Mask reduction rate in each row is 0, 6, 10, 20, and 30% from *Top* to *Bottom*, respectively. Black arrow indicates the best match between measured and simulated distances. Black frame indicates the mask reduction rate that is used for further analysis.

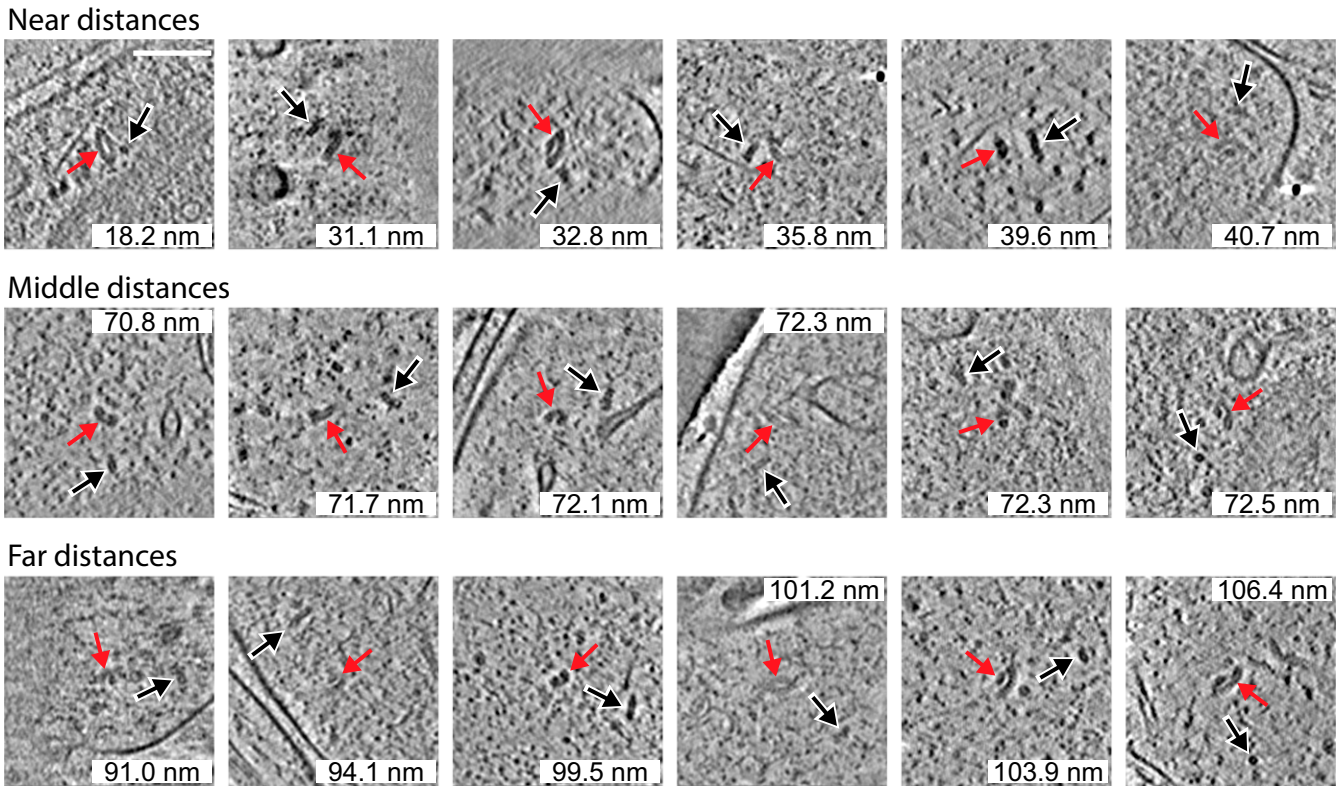

Fig. S9. Examples of TPPII and 26S proteasome pairs. The panels show several examples of TPPII and 26S proteasome pairs in near distance, middle distance, and far distance. Red arrows indicate TPPII. Black arrows indicate 26S proteasome. (Scale bar, 100 nm.)